

Long-legged Divertors and Neutral Baffling as a Solution to the Tokamak Power Exhaust Challenge

K. Verhaegh¹, J.R. Harrison¹, D. Moulton¹, B. Lipschultz², N. Lonigro^{2,1}, N. Osborne^{3,1}, P. Ryan¹, C. Theiler⁴, T. Wijkamp^{5,6}, D. Brida⁷, C. Cowley^{2,1}, G. Derks^{6,5}, R. Doyle⁸, F. Federici^{9,1}, B. Kool^{6,5}, O. Février⁴, A. Hakola¹⁰, S. Henderson¹, H. Reimerdes⁴, A.J. Thornton¹, N. Vianello¹¹, M. Wischmeier⁷, L. Xiang¹ and the EUROfusion Tokamak Exploitation Team* and the MAST Upgrade Team**

¹ United Kingdom Atomic Energy Authority, Culham, United Kingdom

² York Plasma Institute, University of York, United Kingdom

³ University of Liverpool, Liverpool, United Kingdom

⁴ Swiss Plasma Centre, École Polytechnique Fédérale de Lausanne, Lausanne, Switzerland

⁵ Eindhoven University of Technology, Eindhoven, The Netherlands

⁶ Dutch Institute for Fundamental Energy Research DIFFER, Eindhoven, The Netherlands

⁷ Max Planck Institute for Plasma Physics, Garching, Germany

⁸ Dublin City University, Dublin, Ireland

⁹ Oak Ridge National Laboratory, Oak Ridge, United States

¹⁰ VTT Technical Research Centre of Finland, Espoo, Finland

¹¹ Consorzio RFX, Padova, Italy

* See the author list of “Overview of the EUROfusion Tokamak Exploitation programme in support of ITER and DEMO” by E. Joffrin Nuclear Fusion 2024 10.10788/1741-4326/ad2be4.

** See the author list of “Overview of physics results from MAST Upgrade towards core-pedestal-exhaust integration” by J.R. Harrison et al. to be published in Nuclear Fusion Special Issue: Overview and Summary Papers from the 29th Fusion Energy Conference (London, UK, 16-21 October 2023).

E-mail: kevin.verhaegh@ukaea.uk

Abstract.

Exhausting the power from the hot fusion core to the plasma facing components is one of fusion’s biggest challenges. The MAST Upgrade tokamak uniquely integrates strong containment of neutrals within the exhaust area (divertor), away from the hot fusion core, with extreme divertor shaping. This enables improving power exhaust through long-legged divertors with a high magnetic field gradient (total flux expansion). This study shows compelling MAST-U results for the improved power exhaust of long-legged, totally flux expanded, divertors, without any adverse impact to the hot fusion core, representing a significant step forward in addressing the fusion power exhaust challenge. Our comparative analysis of various divertor shapes demonstrates that even modest adjustments can significantly enhance exhaust performance while preserving core

plasma performance. Through novel analysis, we attribute the reductions in particle and power loads to the expanded plasma-neutral interaction volume within long-legged divertors, in agreement with reduced models and simulation results. Strong segregation of neutrals enables the benefits of long-legged, totally flux expanded, divertors to be retrieved. Our study underscores the critical role of strategic divertor shaping in enhancing exhaust performance, stability and core-edge integration; signifying an essential advancement towards sustainable fusion energy.

Keywords: Nuclear Fusion; Tokamak; Alternative Divertor Configurations; MAST Upgrade; Super-X divertor; Plasma detachment

1. Addressing the power exhaust challenge in nuclear fusion: exploring alternative divertor configurations

The pursuit of nuclear fusion as a sustainable energy source faces a significant hurdle: power exhaust [1, 2]. In this study, we present experimental findings from the MAST Upgrade tokamak aimed at addressing this critical challenge.

In magnetic confinement fusion, encompassing tokamaks and stellarators [3], the fusion plasma is confined within nested, closed flux surfaces. However, the heat and particles generated within the plasma are expelled into the open flux surfaces forming the Scrape-Off Layer (Figure 1). Using coils to introduce a magnetic null ('X-point'), the heat and particle fluxes following the open field lines are redirected into a dedicated region - 'the divertor' (Figure 1). The narrow SOL width results in immense target heat fluxes ($150 \text{ MW}/\text{m}^2$ for the DEMO reactor design [1, 2]), far exceeding engineering limits ($5\text{-}10 \text{ MW}/\text{m}^2$ [1, 2]) if unmitigated. Compact reactor designs like STEP, SPARC, and ARC [4–6] face an even larger power exhaust challenge.

Plasma detachment is crucial to mitigate these heat fluxes and occurs at electron temperatures $\leq 5 \text{ eV}$. A collection of plasma-atom/molecule interactions result in simultaneous power, particle, and momentum losses (see Methods section); reducing ion target fluxes and physically 'detaching' the 'hot', ionising plasma ($> 4 \text{ eV}$) from the target. Advanced spectroscopic analysis techniques [7] can reveal the interactions at play, showing that Molecular Activated Recombination (MAR) and Electron-Ion Recombination (EIR) form downstream of the ionisation region after detachment (Figure 1(c,d)).

Uncertainties persist whether target heat fluxes can be sufficiently mitigated whilst maintaining fusion core performance using conventional (detached) divertor strategies [2, 10]. Various alternatives have been proposed, including (combinations of) liquid metal targets [11, 12], high impurity injection to induce X-point radiators [13–15], and using coils to optimise the divertor shape into Alternative Divertor Configurations (ADCs) [16–18]. ADCs aim to reduce heat loads [16], improve detachment access, increase its operational window [19, 20] and improve control over the detachment front [20] by reducing its sensitivity to changes in core parameters (see Methods section).

Examples of ADCs include long-legged divertors, achieved by increasing the distance between the X-point and the target [18, 21], as well as spreading the power over a larger

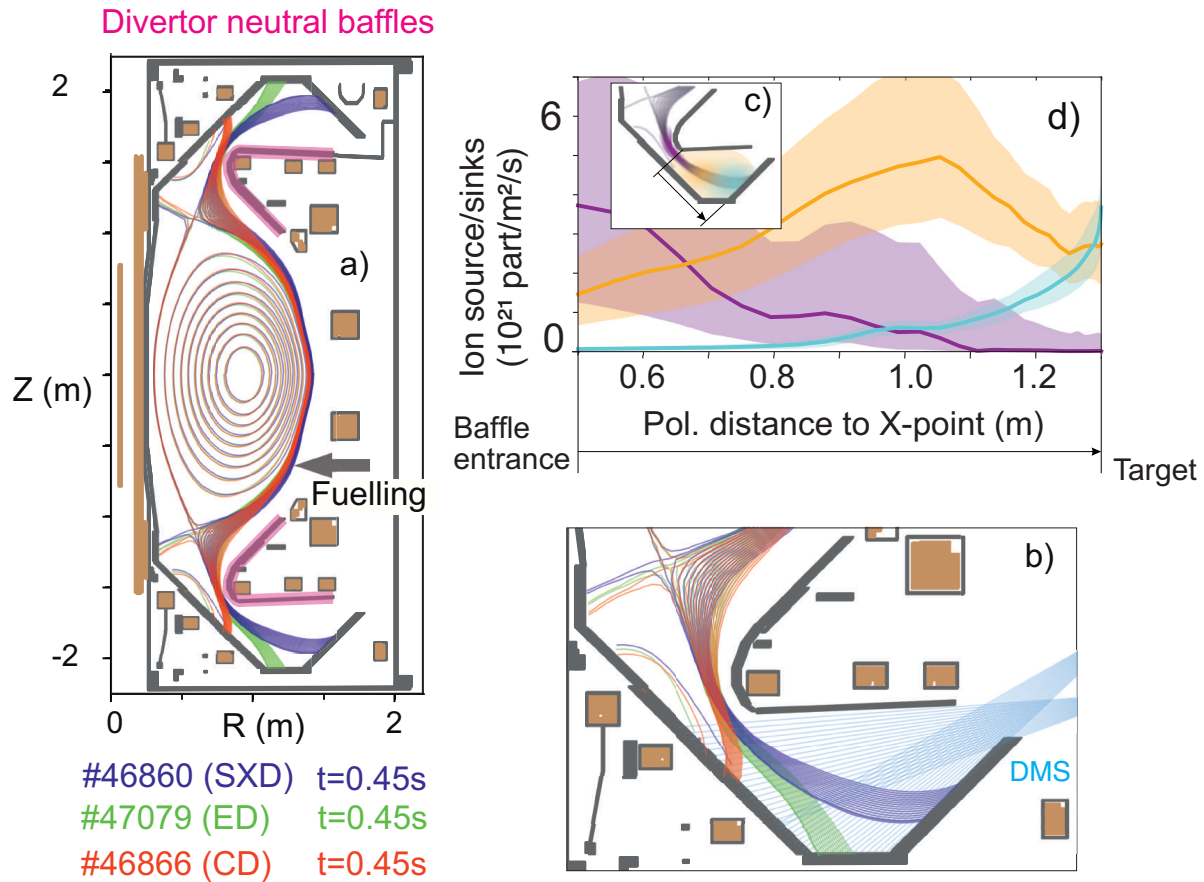


Figure 1. Overview of MAST-U plasma shapes, coil positions, combined with an overview of the plasma processes in the MAST-U divertor. (a) Overview of the magnetic geometry for the Super-X Divertor (SXD), Elongated Divertor (ED) and, Conventional Divertor (CD), with an indication of the fuelling and divertor neutral baffle location. (b) Zoom-in of the lower divertor with diagnostic coverage of the divertor spectrometer [8,9]. (c) Schematic illustration of the characteristic processes in a detached MAST-U Super-X divertor. (d) 1D profile of the, spectroscopically, line-integrated inferences of the divertor ion sources and sinks as function of poloidal distance from the X-point to the target for the Super-X divertor, indicating the ionisation front position (# 46860, 45 % Greenwald fraction).

area at the target by increasing the spacing between magnetic flux surfaces ('poloidal flux expansion') and/or by increasing the magnetic field gradient between the X-point and the target ($F_R = \frac{B_t}{B_{xpt}}$): 'total flux expansion' (see Methods section). The neutrals generated from ions recombining at the target or volumetrically can be contained in the divertor chamber by introducing divertor baffle plates (Figure 1(a,b)). This intensifies divertor plasma-neutral interactions and reduces the transport of divertor neutrals to the core [21–23], improving the compatibility between a detached divertor and improved core performance.

MAST Upgrade is the UK's national fusion experiment that has been newly built (2021) to tackle one of fusion's greatest challenges: power exhaust, by uniquely integrating strong neutral baffling, long-legged divertors (divertor leg length / major radius > 1),

and high total flux expansion (up to 2.5). In contrast, conventional divertor solutions (on JET, Asdex-Upgrade [24]) have short-legged divertors (divertor leg length / major radius < 0.1), negligible total flux expansion ($F_R \sim 1$) and no neutral baffles.

This work provides seminal results from MAST-U's ability to tackle power exhaust by using its spherical nature ('apple-shaped') to enable extreme divertor shape variations. This facilitates F_R variations over a much larger range (1-2.5) than possible in conventional ('doughnut-shaped') tokamaks with flexible shaping, such as TCV (1-1.6). Preliminary MAST-U results under low power conditions ($P_{\text{SOL}} = 0.4$ MW) demonstrate the benefits of the 'Super-X Divertor (SXD)' [25,26], which has the highest F_R achievable, over the conventional divertor ($F_R = 1.2$) [8, 19, 27]; consistent with simulations [19]. Instead of focussing on these two extremes, in this study we utilise MAST-U's flexibility to systematically investigate the impact of total flux expansion and divertor leg length in plasmas with external heating (1.5-1.7 MW Neutral beam heating, $P_{\text{SOL}} = 1.2$ MW). First, we present the strongest experimental evidence to date for the benefits of combined total flux expansion and divertor leg length. Secondly, we investigate the physics of such divertors using novel analysis techniques and comparisons with reduced and full-models. Thirdly, we discuss how these findings relate to the field and form a milestone towards ADC design for future reactors [4, 28, 29].

2. Benefits of total flux expansion and divertor leg length under strong neutral baffling

By systematically comparing three divertor geometries: the Conventional Divertor (CD); Elongated Divertor (ED) and Super-X Divertor (SXD) (Figure 1, divertor shape parameters shown in table 8), we find five benefits of combined total flux expansion, poloidal leg length and divertor neutral baffling. For each divertor configuration, the evolution of their power exhaust and detachment properties are diagnosed as the core electron density is gradually increased, whilst other parameters are held as constant as possible, resulting in colder, and more detached, divertor conditions.

- (i) Improved access to detachment.
- (ii) Increased operational regime for detached divertor operation.
- (iii) Improved detachment stability.
- (iv) Reduced target heat fluxes and power loads.
- (v) Divertor detachment enabled without adverse core impact.

These improved performance of combined total flux expansion and poloidal leg length are driven by differences in divertor shape, according to our analysis (section 3.1), consistent with reduced model (section 3.2) and simulation (section 3.3). Maintaining this strong neutral baffling is key to retrieving the benefits of the divertor shape (section 4).

In the CD, the integrated target particle fluxes (Figure 2a) increase as function of core density, indicative of an attached discharge, up to a core Greenwald fraction of

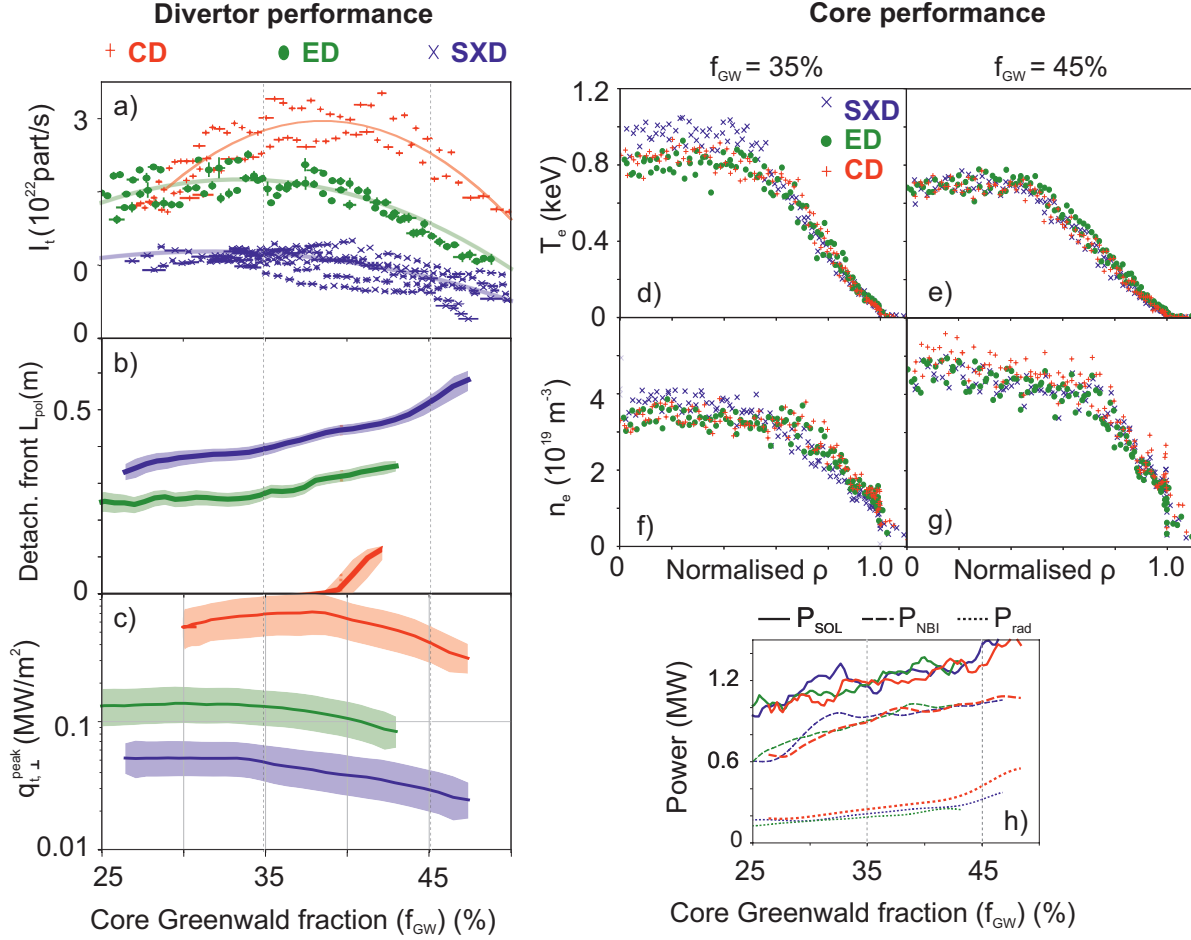


Figure 2. Overview of lower outer divertor parameters (a,b,c) and of core parameters (d,e,f,g,h) in the CD (red), ED (green) and SXD (blue) as function of core Greenwald fraction (f_{GW} in %). Divertor parameters: (a) Integrated ion target flux (with polynomial fits), (b) detachment (ionisation) front position, (c) estimated perpendicular target heat load combining Langmuir probe and spectroscopy measurements [8, 9]. Core parameters: (d-g) core electron temperatures and densities at two different core Greenwald fractions (corresponding to vertical dotted lines in (a-c)), (h) P_{SOL} (solid lines) deduced from the following contributors: NBI absorption (TRANSP, dashed lines); Ohmic heating (EFIT, not shown); changes to stored energy (EFIT, not shown) and core radiative losses (bolometry, dotted lines).

$f_{GW} \approx 40\%$. At this point, both the particle flux at the target decreases and the ionisation front detaches from the target (Figure 2b), indicative of the onset of detachment. In contrast, the ED and SXD are detached throughout the scanned core density range: the ionisation front remains detached from the target and the particle flux does not increase with increasing density. *The longer legged, totally flux expanded, divertors thus have improved access to detachment compared to the CD.* Since there is no difference in the density limit achievable between the different geometries, *the operational window for detached operation is increased for the long-legged divertors, compared to the CD.*

The sensitivity of the detachment front to changes in core density, i.e, the slope of the

detachment front position (Figure 2(b)), at the CD detachment onset point ($f_{GW} \approx 40\%$) is a factor 5 steeper for the CD, compared to the ED and SXD. This suggests that perturbations in core density result in a larger movement of the detached region in the CD, compared to the ED and SXD, leading to a rapid movement of the ionisation region out of the divertor chamber after detachment. This coincides with an increase in core radiation (Figure 2). *The longer-legged with increased total flux expansion have a higher detachment stability to slow, steady-state, perturbations*, which is qualitatively consistent with reduced models [20].

Based on the magnetic geometry [16], a reduction in perpendicular heat flux by $\sim 5.1\times$ and $\sim 2.5\times$ for the SXD and ED is expected, compared to the CD, due to increased poloidal ($\sim 2.7\times$ (SXD) and $\sim 1.8\times$ (ED)) and total ($\sim 1.9\times$ (SXD) and $\sim 1.4\times$ (ED)) flux expansion. However, a much larger reduction in target heat flux is observed: $\sim 18.5\times$ and $\sim 7\times$ for the SXD and ED, compared to the CD (Figure 2 c). This suggests that the longer-legged divertors result in *additional heat flux dissipation* through volumetric and/or cross-field transport by a factor $\sim 3.6\times$ (SXD) and $\sim 2.8\times$ (ED), beyond heat flux spreading at the target due to the magnetic geometry. This is consistent with both SOLPS-ITER simulations (section 3.3) [19] and volumetric power loss estimates (section 3.1).

The core densities, temperatures and P_{SOL} are the same for the CD, ED and SXD (Figure 2(d-h)). These results indicate a strong decoupling between the divertor shape and the obtained core conditions the outer target being detached. Therefore, *the combined total flux expansion and poloidal leg length enables divertor detachment without adverse core impact*, in contrast to the CD - which needs high densities to detach ($f_{GW} > 40\%$) at which the core radiation is increased.

3. What drives the physics of long-legged, strongly baffled, divertors?

After having shown the benefits of strong baffled, long-legged, totally flux-expanded, divertors, we will explore why these divertors have a superior exhaust performance using novel spectroscopic analysis [7]. This shows similar ion sources/sinks between the different shapes *as function of poloidal distance to the X-point*: the additional volume in the SXD and ED, compared to the CD, results in their superior power dissipation and drives the reduction of the ion target flux during detachment through ion sinks. This result is consistent with reduced model predictions as well as SOLPS-ITER exhaust simulations.

3.1. Power and particle balance shows benefit long-legged divertors driven by additional volume

Comparing particle balance for all three divertors shows the *total ion source*, inferred through particle balance, is *similar* between the different geometries, within uncertainties. Meanwhile, the *reduced target fluxes in the SXD and ED* are driven by *increased ion*

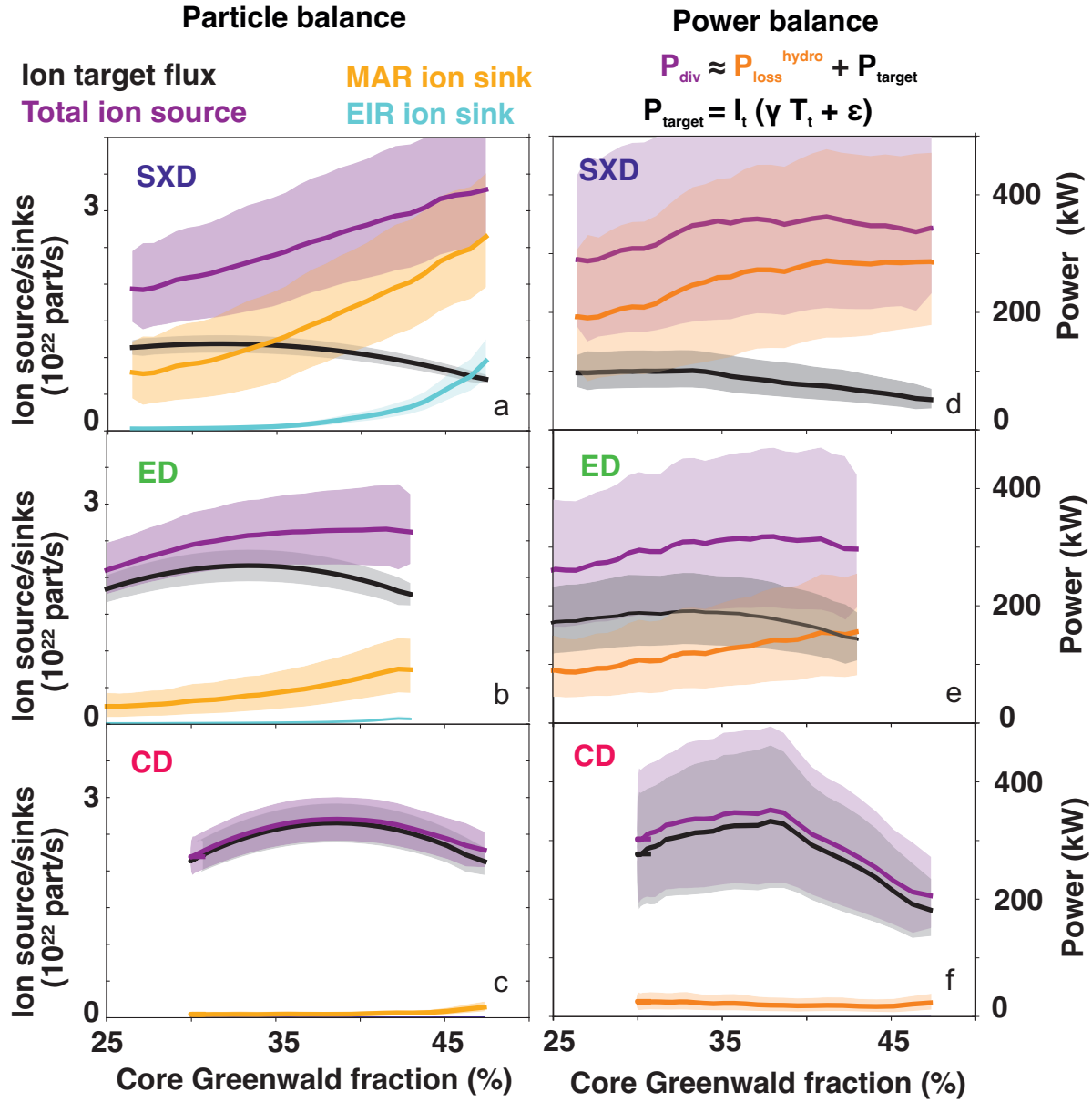


Figure 3. Overview of divertor particle (a-c) and power (d-f) balance in the lower outer divertor for the SXD, ED and CD configurations as function of core density. (a-c) Integrated particle balance showing the ion target flux, total ionisation source, MAR ion sink and EIR ion sink. (d-f) Integrated power balance showing hydrogenic power losses, target power deposition and estimated power flow into the divertor chamber.

sinks (3(a,b,c)). Ion sinks are significant in both the SXD and the ED from the start of the discharge, both through MAR (in the SXD and ED) as well as EIR (in the SXD) integrated throughout the divertor chamber. Our spectroscopic analysis reveals plasma conditions of $n_e = 2 - 4 \times 10^{19} m^{-3}$ and $T_e \approx 0.2$ eV in the region where EIR becomes observable ($f_{GW} > 33\%$ in the SXD and $f_{GW} > 40\%$ in the ED) [27, 30]. MAR only appears in the CD at the highest core densities after its ionisation front detaches from the target ($f_{GW} > 40\%$), but its magnitude remains limited as the spatial region over

which the CD is detached downstream of the baffle is limited.

Analogously, the inferred power flowing into the divertor chamber (plasma target power load plus volumetric power loss) is similar for all three geometries (Figure 3): the reduction in target power loads in the SXD and ED arises from additional volumetric power dissipation in their divertor volume (Figure 3 (d-f)). As the inferred hydrogenic radiation is similar to the total measured radiation from an imaging bolometer (not shown) [9, 31], the divertor power losses mostly arises from hydrogenic processes. These hydrogenic power losses lower the integrated target power load by a factor $\sim \times 4$ (SXD) and $\sim \times 2$ (ED), compared to the CD; consistent with the observed reduction of target heat loads Figure 2(c). A significant part of these power losses originate from Molecular Activated Dissociation (MAD) in the detached region of the plasma, resulting in neutrals that mostly re-associate at the side-walls according to exhaust simulations. This mostly contributes to the reduction of target power load between the SXD and ED, illustrating that power losses can be significantly enhanced in detached conditions by accessing even deeper detachment.

Further insight into power and particle balance is obtained by studying the 1D profiles of ion sources and sinks (a-c), as well as power flows (g), along the divertor leg *as function of poloidal distance to the X-point* in figure 4 at a fixed core density ($f_{GW} = 35\%$). The ion sources and sinks, as well as power flow, profiles are similar between the different geometries (up until the CD detachment onset) *at the same poloidal distance to the X-point*. This suggests the plasma is predominantly altered in the extended region of the SXD and ED, compared to the CD, which explains why the core parameters are the same between the three geometries. The deeper detachment and lower power loads in the SXD and CD are brought on by interactions in the additional volume available downstream of the ionisation region when the divertor leg is extended.

3.2. Reduced models suggest detachment onset reduction driven by shape differences

To gain further insights into what drives the differences in detachment onset between the different divertor configurations, the experimental results are compared against the Detachment Location Sensitivity (DLS) analytical model [20, 32, 33]. The detachment threshold ($C_t \propto \frac{f_{GW}}{P_{SOL}^{5/7}}$ - see Methods section) is a function of the magnetic geometry, which mostly depends on total flux expansion (F_R), connection length (L_{\parallel}) and the averaged magnetic field strength $\langle B \rangle$: $C_t \propto \frac{1}{F_R} \left(\frac{B_{xpt}}{\langle B \rangle} \right)^{2/7} \frac{1}{L_{\parallel}^{2/7}}$.

According to the DLS model, the detachment threshold is reduced by 43 and 56 % for the ED and SXD compared to the CD, mostly due to an increased F_R . Since the CD detaches near $f_{GW} \approx 40\%$ ($T_e \approx 4$ eV), the SXD and ED are predicted to attach at $f_{GW} < 20\%$. This is consistent with the experiment where both geometries remain detached for the entire experiment ($f_{GW} > 25\%$ - figure 2 (a-c)). To compare the SXD against the ED, a colder reference point must be tracked. EIR appears at the target at a 30 % higher f_{GW} for the ED compared to the SXD (figure 3 (a,b)), consistent with a DLS model predicted 33 % increase in f_{GW} for the detachment onset. The lack of EIR

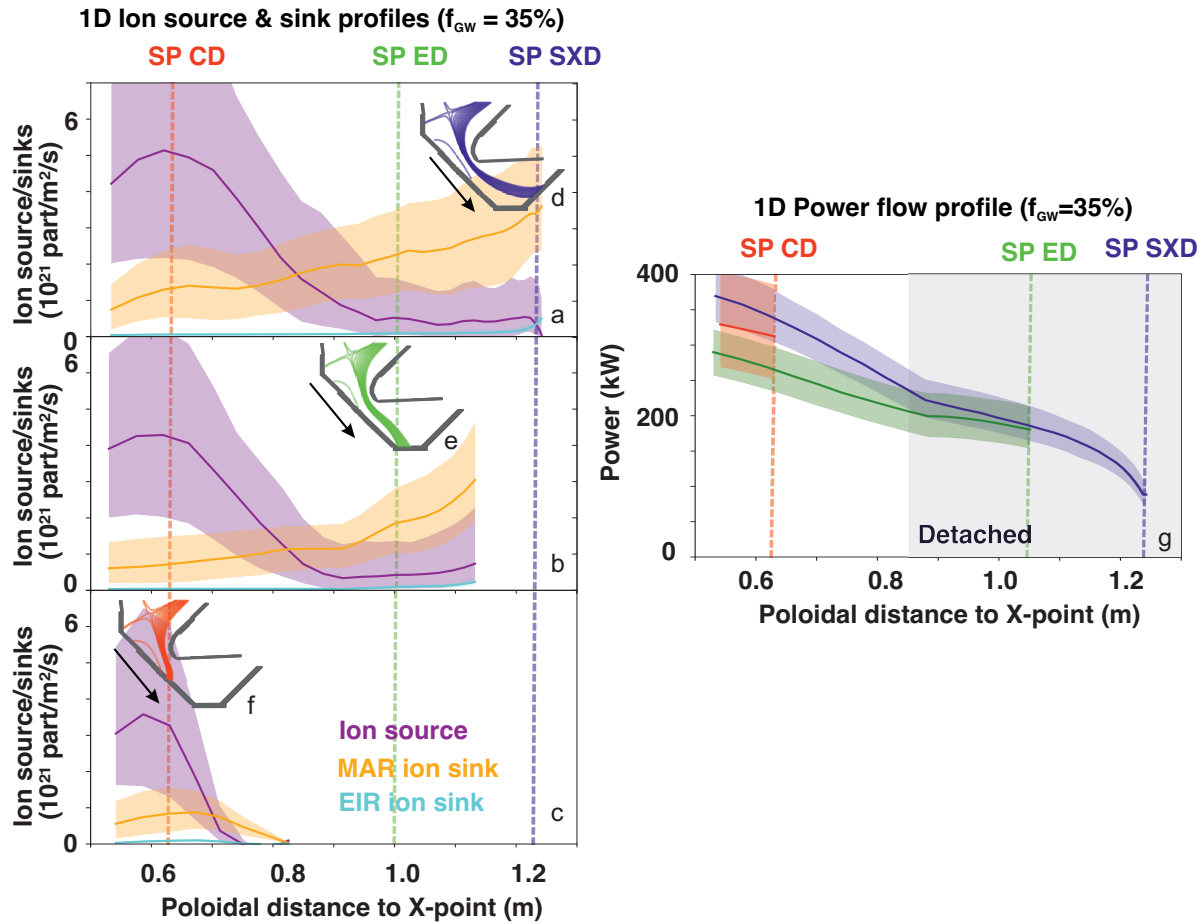


Figure 4. Ion source/sink and power flow profiles at $f_{GW} = 35\%$ as function of poloidal distance to X-point show additional length SXD and ED drives power losses and deepens detachment. Spectroscopically inferred ion sources and sinks for the SXD (a), ED (b) and CD (c) with coloured dotted lines indicating their respective strike point position, indicated by their magnetic geometry (d-f). (g) Power flow inferred from power balance from the divertor entrance towards the target for the CD (red), ED (green) and SXD (blue), with a dotted line indicating their respective strike points. The part where the divertor leg is detached is indicated in grey.

in the CD is consistent with the DLS model which, given the f_{GW} at which EIR appears in the SXD, predicts the onset of EIR in the CD at higher densities than obtained experimentally ($f_{GW} = 68\%$, Figure 6(b)).

The impact of total flux expansion on detachment onset predicted by the DLS model is consistent with our experimental observations. Although the additional volume in the SXD and ED is critical to explain the *reduction of target power and particle loads*, this suggests that *total flux expansion* drives their detachment onset reductions.

3.3. Comparison of strike point scan to exhaust simulations

The results in figure 2(b) suggested that the ionisation front position, once detached from the target, is insensitive to the magnetic topology downstream of it: its location

depends only on the upstream magnetic topology, consistent with DLS predictions. This is further investigated by slowly sweeping the outer strike point from a CD to an ED to a SXD geometry at a constant density (30 % Greenwald fraction, $n_e^{sep} \approx 0.8 \times 10^{18} m^{-3}$) and power ($P_{SOL} \approx 1.0$ MW).

The evolution of the D_2 Fulcher band emission, which is a proxy for the ionisation source [8, 34], is shown in figure Figure 5 (d-f). Once the D_2 Fulcher emission front is observed to detach from the target ($r \approx 0.95$ m), the position of the ionisation front remains close to this radius throughout the strike point scan. This further illustrates that the ionisation front position is insensitive to the magnetic topology downstream of it, consistent with the DLS model.

This behaviour agrees with SOLPS-ITER predictions [19] of the CD, ED and SXD configurations (Figure 5 a-c). The CD simulation is attached, whereas the SXD and ED simulations are detached. The radius of both the D_2 Fulcher emission front as well as the 5 eV contour, for the ED and SXD, remains near $r = 0.95$ m.

A more detailed comparison between experiments and simulations is obtained by comparing their ion sources and sinks (Figure 5 (g-i)), indicating a quantitative agreement between experiments and simulations for the ion source and EIR. The MAR ion sinks are underestimated in the simulation in the low temperature regime, far down the ionisation region. This discrepancy is resolved when a corrected rate molecular charge exchange rate is used in SOLPS-ITER, adopted from [27] (Figure 5 (g)).

4. The importance and relevance of our findings

Both simulations and experiments indicate that the neutral pressures and neutral trapping [26] is similar between the three divertor geometries. This, combined with the finding that 1) the MAST-U results agree with the DLS model that only considers the plasma's magnetic geometry; 2) that the upstream parameters are invariant to the magnetic topology downstream, implies that the improved exhaust performance of the SXD, ED and CD is *driven by divertor shape*, rather than *differences* in neutral baffling. However, as will be shown from comparisons with other results, strong baffling *enables* the benefits of long-legged, totally flux expanded, divertors to be retrieved.

4.1. Comparison with results on other devices

The benefits of long-legged divertors, total flux expansion, divertor shaping and neutral baffling have been individually studied on TCV [16, 18]. These results showed neutral baffling improved power exhaust [22], increased neutral compression, and improved core-edge integration [35]. TCV results indicated signs of enhanced detachment stability of the X-Divertor (factor 1.8 \times) and X-Point Target (factor 1.2 \times) divertors [16] indicated signs of enhanced detachment stability, observed more strongly (factor 5 \times) in the long-legged, totally flux expanded, MAST-U SXD and ED (Figure 2(b)).

MAST-U [36, 37], with its unique capabilities, is able to combine strong baffling and

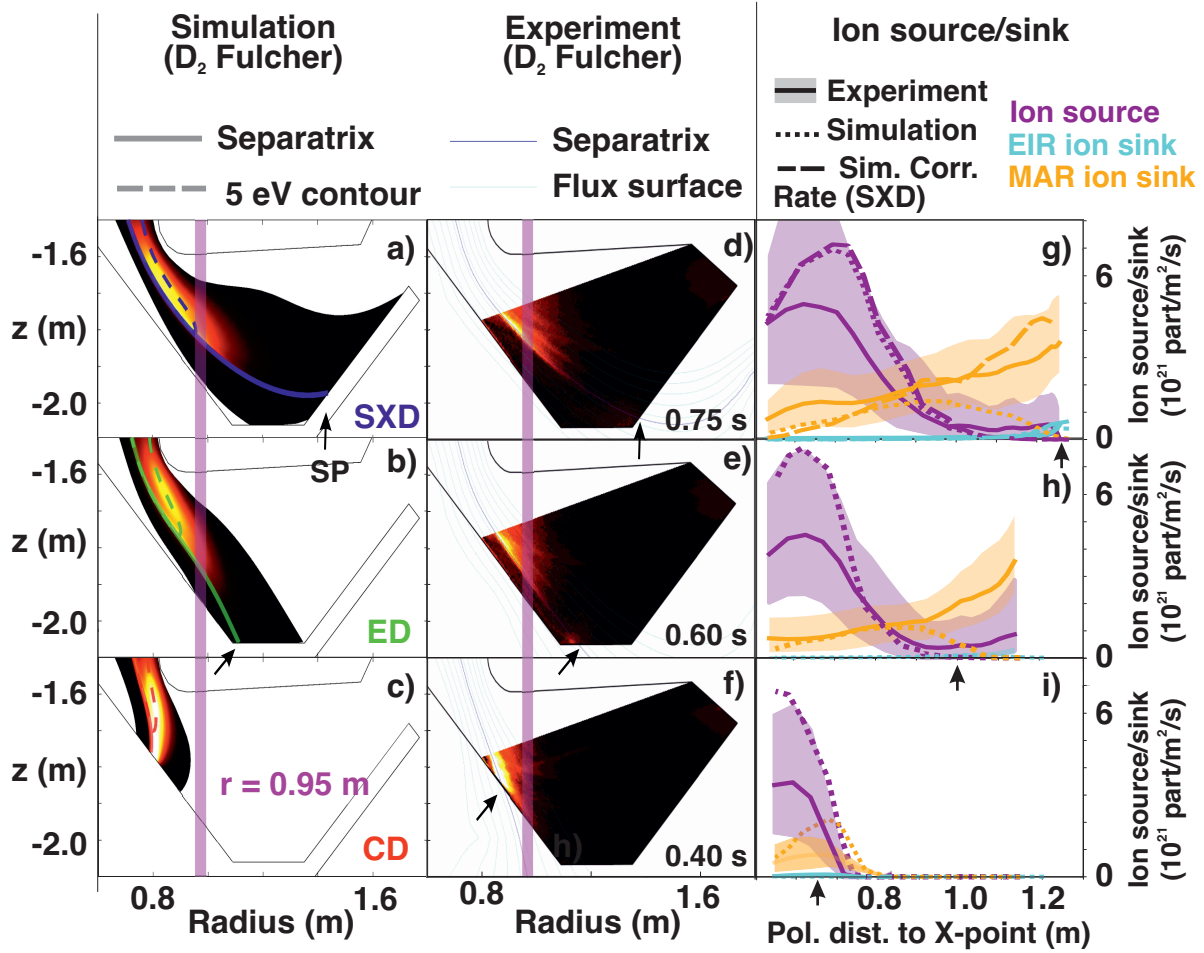


Figure 5. Experiment to simulation comparison. (a-c) D_2 Fulcher emission from SOLPS-ITER simulations for the CD, ED and SXD. The synthetic D_2 Fulcher emission (colour map) is indicative of the ionisation region and is overlaid with 5 eV contours (dotted lines). (d-f) Experimentally measured D_2 Fulcher band emission (595-605 nm) for a strike point scan, moving from CD to SXD at constant density and power, obtained through inverting MWI imaging data for # 46895. To guide the eye, a magenta vertical line has been added at a radius of 0.95 m (a-f) and an arrow has been added at the strike point location (a-i). (h-i) 1D ion sources and sinks obtained from spectroscopic analysis (figure 4 (a-c)) compared against synthetic diagnostic results from SOLPS-ITER simulations (dotted lines). For the SXD (g) two SOLPS-ITER simulation results are shown: one with default rates and one with corrected molecular charge exchange rates 'Sim. Corr. Rate' obtained from [27].

extreme divertor shaping to test the integration of novel divertor solutions under strongly baffled conditions. The DLS detachment onset predictions (in terms of upstream density, P_{SOL} and impurity concentration) varies by 110 % from CD to SXD. Comparatively, the modelled DLS detachment onset predictions for a range of TCV divertor geometries (target radius scan, poloidal flux expansion scan, as well as for the X-point target divertor) [16, 18] varies over 70 % (Figure 7).

The benefit of total flux expansion on TCV is smaller than predicted by the DLS

model [38, 39]. SOLEDGE2D-EIRENE simulations suggests that the neutral baffling on TCX may be insufficient to recover the benefit of total flux expansion [40], consistent with previous SOLPS-ITER simulations [26]. The lack of strong baffling results in strong plasma flows from the midplane to the target due to neutrals escaping the divertor [41], which can diminish the impact of total flux expansion on the detachment onset [38]. Hence, by integrating strong baffling, long-legged divertors and total flux expansion, MAST-U enables retrieving the full benefit of its extreme shaping capability (Figure 7).

4.2. Implications for reactors

The validation of both reduced models and exhaust simulations, using the unique capabilities of MAST-U as a test bed for investigating novel divertor topologies, reduces uncertainty in extrapolating current knowledge to reactor class devices. This is a crucial milestone for exploring ADCs as a risk mitigation strategy. Plasma-molecular interactions, and the critical role they play in the ED and SXD, are one example where model validation has illuminated discrepancies (Figure 5 (h)) that have been reduced with improved rates for $D_2 + D^+ \rightarrow D_2^+ + D$. Extrapolating these improved rates to reactors with long-legged, tightly baffled, divertors shows they can make a critical impact on the reactor scale [27]. Additional experiments at higher power (and higher divertor densities) would improve our understanding of how alternative divertors scale with power and are affected by transients, which is an important focus of future MAST-U experiments [42].

Any reactor requires an integrated core-edge scenario, and one concern for using ADCs is that the deep detached conditions of an ADC may impact core conditions. Our work proves that this is not the case in strongly baffled conditions where core-edge compatibility is improved.

One drawback of some ADCs, including the Super-X divertor, in reactors is that their engineering will be more complex and more costly, due to the additional constraints on space, coils, and magnetic control tolerances [28, 43]. A key finding of our research is that smaller changes in the divertor topology (ED vs SXD) can already strongly improve the exhaust performance, in agreement with reduced model predictions and exhaust simulations. This paves the way for reactor ADC designs with improved power exhaust and core-edge compatibility, which require less space and have a reduced engineering complexity.

5. Data availability statement

The data that support these studies are openly available at: <https://doi.org/10.14468/9m0q-kc26>.

To obtain further information on the data and models underlying this paper please contact publicationsmanager@ukaea.uk.

6. Acknowledgements

This work has received support from EPSRC Grants EP/T012250/1 and EP/N023846/1. This work has been carried out within the framework of the EUROfusion Consortium, partially funded by the European Union via the Euratom Research and Training Programme (Grant Agreement No 101052200 — EUROfusion). The Swiss contribution to this work has been funded by the Swiss State Secretariat for Education, Research and Innovation (SERI). Views and opinions expressed are however those of the author(s) only and do not necessarily reflect those of the European Union, the European Commission or SERI. Neither the European Union nor the European Commission nor SERI can be held responsible for them.

7. References

- [1] Wenninger R, Bernert M, Eich T, Fable E, Federici G, Kallenbach A, Loarte A, Lowry C, McDonald D, Neu R *et al.* 2014 *Nuclear Fusion* **54** 114003
- [2] Zohm H, Militello F, Morgan T, Morris W, Reimerdes H and Siccinio M 2021 *Fusion Engineering and Design* **166** 112307 ISSN 0920-3796 URL <https://www.sciencedirect.com/science/article/pii/S0920379621000831>
- [3] Effenberg F, Brezinsek S, Feng Y, König R, Krychowiak M, Jakubowski M, Niemann H, Perseo V, Schmitz O, Zhang D, Barbui T, Biedermann C, Burhenn R, Buttenschön B, Kocsis G, Pavone A, Reimold F, Szepesi T, Frerichs H, Gao Y, Hergenbahn U, Kwak S, Otte M, Pedersen T S and Team W X 2019 *Nuclear Fusion* **59** 106020 URL <https://dx.doi.org/10.1088/1741-4326/ab32c4>
- [4] Hudoba A, Newton S, Voss G, Cunningham G and Henderson S 2023 *Nuclear Materials and Energy* **35** 101410 ISSN 2352-1791 URL <https://www.sciencedirect.com/science/article/pii/S2352179123000492>
- [5] Kuang A Q, Ballinger S, Brunner D, Canik J, Creely A J, Gray T, Greenwald M, Hughes J W, Irby J, LaBombard B and et al 2020 *Journal of Plasma Physics* **86** 865860505
- [6] Wigram M R K, Labombard B, Umansky M V, Kuang A Q, Golfinopoulos T, Terry J L, Brunner D, Rensink M E, Ridgers C P and Whyte D G 2019 *Nuclear fusion* **59** 106052
- [7] Verhaegh K, Lipschultz B, Harrison J, Duval B, Fil A, Wensing M, Bowman C, Gahle D, Kukushkin A, Moulton D, Perek A, Pshenov A, Federici F, Février O, Myatra O, Smolders A, Theiler C, the TCV Team and the EUROfusion MST1 Team 2021 *Nuclear Fusion* **61** 106014 URL <https://doi.org/10.1088/1741-4326/ac1dc5>
- [8] Verhaegh K, Lipschultz B, Harrison J, Osborne N, Williams A, Ryan P, Allcock J, Clark J, Federici F, Kool B, Wijkamp T, Fil A, Moulton D, Myatra O, Thornton A, Bosman T, Bowman C, Cunningham G, Duval B, Henderson S, Scannell R and the MAST Upgrade team 2022 *Nuclear Fusion* **63** 016014 URL <https://dx.doi.org/10.1088/1741-4326/aca10a>
- [9] Verhaegh K, Lipschultz B, Harrison J R, Federici F, Moulton D, Lonigro N, Kobussen S P, O'Mullane M, Osborne N, Ryan P, Wijkamp T, Kool B, Rose E, Theiler C and Thornton A J 2023 *Nuclear Fusion* URL <http://iopscience.iop.org/article/10.1088/1741-4326/acf946>
- [10] Pitts R, Bonnin X, Escourbiac F, Frerichs H, Gunn J, Hirai T, Kukushkin A, Kaveeva E, Miller M, Moulton D, Rozhansky V, Senichenkov I, Sytova E, Schmitz O, Stangeby P, De Temmerman G, Veselova I and Wiesen S 2019 *Nuclear Materials and Energy* **20** 100696 ISSN 2352-1791 URL <https://www.sciencedirect.com/science/article/pii/S2352179119300237>
- [11] Van Eden G, Kvon V, Van De Sanden M and Morgan T 2017 *Nature communications* **8** 192
- [12] Lore J D, Islam M S, Kessel C E, Curreli D, Maingi R, Rezazadeh M and Smolentsev S 2022 *IEEE Transactions on Plasma Science* **50** 4199–4205

- [13] Stroth U, Bernert M, Brida D, Cavedon M, Dux R, Huett E, Lunt T, Pan O, Wischmeier M *et al.* 2022 *Nuclear Fusion* **62** 076008
- [14] Pan O, Bernert M, Lunt T, Cavedon M, Kurzan B, Wiesen S, Wischmeier M and Stroth U 2022 *Nuclear Fusion*
- [15] Lunt T, Bernert M, Brida D, David P, Faitsch M, Pan O, Stieglitz D, Stroth U, Redl A, Team A U *et al.* 2023 *Physical Review Letters* **130** 145102
- [16] Theiler C, Lipschultz B, Harrison J, Labit B, Reimerdes H, Tsui C, Vijvers W A J, Boedo J A, Duval B P, Elmore S, Innocente P, Kruezi U, Lunt T, Maurizio R, Nespoli F, Sheikh U, Thornton A J, van Limpt S H M, Verhaegh K, Vianello N, Team T and Team E M 2017 *Nuclear Fusion* **57** 072008 ISSN 0029-5515 URL <http://iopscience.iop.org/article/10.1088/1741-4326/aa5fb7/pdf>
- [17] Ryutov D D and Soukhanovskii V A 2015 *Physics of Plasmas* **22** 110901 ISSN 1070-664X (*Preprint* https://pubs.aip.org/aip/pop/article-pdf/doi/10.1063/1.4935115/14865569/110901_1_online.pdf) URL <https://doi.org/10.1063/1.4935115>
- [18] Reimerdes H, Duval B P, Harrison J R, Labit B, Lipschultz B, Lunt T, Theiler C, Tsui C K, Verhaegh K, Vijvers W A J, Boedo J A, Calabro G, Crisanti F, Innocente P, Maurizio R, Pericoli V, Sheikh U, Spolare M, Vianello N, the T C V t and the E M S T t 2017 *Nuclear Fusion* **57** 126007 ISSN 0029-5515 URL <http://stacks.iop.org/0029-5515/57/i=12/a=126007>
- [19] Moulton D *et al.* 2023 *Nuclear Fusion*, submitted
- [20] Lipschultz B, L Para F and Hutchinson I 2016 *Nuclear Fusion* **56** 056007 ISSN 0029-5515 URL <http://stacks.iop.org/0029-5515/56/i=5/a=056007>
- [21] Umansky M, LaBombard B, Brunner D, Golfinopoulos T, Kuang A, Rensink M, Terry J, Wigram M and Whyte D 2019 *Nuclear Fusion* **60** 016004 URL <https://dx.doi.org/10.1088/1741-4326/ab46f4>
- [22] Reimerdes H and et al 2022 *Nuclear Fusion* **62** 042018 URL <https://dx.doi.org/10.1088/1741-4326/ac369b>
- [23] Sang C, Guo H, Stangeby P, Lao L and Taylor T 2017 *Nuclear Fusion* **57** 056043 URL <https://dx.doi.org/10.1088/1741-4326/aa6548>
- [24] Eich T, Sieglin B, Thornton A, Faitsch M, Kirk A, Herrmann A and Suttrop W 2017 *Nuclear Materials and Energy* **12** 84–90 ISSN 2352-1791 proceedings of the 22nd International Conference on Plasma Surface Interactions 2016, 22nd PSI URL <https://www.sciencedirect.com/science/article/pii/S2352179116302927>
- [25] Valanju P M, Kotschenreuther M, Mahajan S M and Canik J 2009 *Physics of Plasmas (1994-present)* **16** 056110
- [26] Fil A, Lipschultz B, Moulton D, Dudson B D, Février O, Myatra O, Theiler C, Verhaegh K, Wensing M and and 2020 *Plasma Physics and Controlled Fusion* **62** 035008
- [27] Verhaegh K, Harrison J R, Lipschultz B, Lonigro N, Kobussen S, Moulton D, Osborne N, Ryan P, Theiler C, Wijkamp T, Brida D, Derks G, Doyle R, Federici F, Hakola A, Henderson S, Kool B, Newton S, Osawa R, Pope X, Reimerdes H, Vianello N and Wischmeier M 2024 *Nuclear Fusion (Preprint NuclearFusion, inpress. arxiv:2311.08580)*
- [28] Militello F, Aho-Mantila L, Ambrosino R, Body T, Bufferand H, Calabro G, Ciraolo G, Coster D, Di Gironimo G, Fanelli P *et al.* 2021 *Nuclear Materials and Energy* **26** 100908 ISSN 2352-1791
- [29] Reimerdes H, Ambrosino R, Innocente P, Castaldo A, Chmielewski P, Gironimo G D, Merriman S, Pericoli-Ridolfini V, Aho-Mantilla L, Albanese R, Bufferand H, Calabro G, Ciraolo G, Coster D, Fedorczak N, Ha S, Kembleton R, Lackner K, Loschiavo V, Lunt T, Marzullo D, Maurizio R, Militello F, Ramogida G, Subba F, Varoutis S, Zagórski R and Zohm H 2020 *Nuclear Fusion* **60** 066030 URL <https://dx.doi.org/10.1088/1741-4326/ab8a6a>
- [30] Lonigro N *et al.* 2023 First 2d electron density measurements using coherence imaging spectroscopy in the mast-u super-x divertor *EPS Conference of Plasma Physics 2023*
- [31] Federici F, Reinke M L, Lipschultz B, Thornton A J, Harrison J R, Lovell J J and Bernert M 2023 *Review of Scientific Instruments* **94** 033502

- [32] Cowley C, Lipschultz B, Moulton D and Dudson B 2022 *Nuclear Fusion* **62** 086046 URL <https://dx.doi.org/10.1088/1741-4326/ac7a4c>
- [33] Myatra O, Lipschultz B, Moulton D, Verhaegh K, Dudson B, Orchard S, Fil A and Cowley C 2023 *Nuclear Fusion* **63** 096018 URL <https://dx.doi.org/10.1088/1741-4326/acea33>
- [34] Wijkamp T, Allcock J, Feng X, Kool B, Lipschultz B, Verhaegh K, Duval B, Harrison J, Kogan L, Lonigro N, Perek A, Ryan P, Sharples R, Classen I, Jaspers R and the MAST Upgrade team 2023 *Nuclear Fusion* **63** 056003 URL <https://dx.doi.org/10.1088/1741-4326/acc191>
- [35] Sheikh U, Dunne M, Frassinetti L, Labit B, Blanchard P, Duval B, Février O, Galassi D, Merle A, Reimerdes H and Theiler C 2021 *Nuclear Materials and Energy* **26** 100933 ISSN 2352-1791 URL <https://www.sciencedirect.com/science/article/pii/S2352179121000259>
- [36] Harrison J *et al.* 2024 *IAEA Fusion Energy Conference, Nuclear Fusion, submitted*
- [37] Morris W, Harrison J, Kirk A, Lipschultz B, Militello F, Moulton D and Walkden N 2018 *IEEE Transactions on Plasma Science* **46** 1217–1226
- [38] Carpita M, Février O, Reimerdes H, Theiler C, Duval B, Colandrea C, Durr-Legoupil-Nicoud G, Galassi D, Gorno S, Huett E, Loizu J, Martinelli L, Perek A, Simons L, Sun G, Tonello E, Wüthrich C and the TCV Team 2024 *Nuclear Fusion* **64** 046019 URL <https://dx.doi.org/10.1088/1741-4326/ad2a2a>
- [39] Février O, Theiler C, Coda S, Colandrea C, de Oliveira H, Duval B, Gorno S, Labit B, Linehan B, Maurizio R, Perek A, Reimerdes H, Wüthrich C and the TCV Team 2021 *Nuclear Fusion* **61** 116064 URL <https://dx.doi.org/10.1088/1741-4326/ac27c6>
- [40] Meineri C, Muscente P, Theiler C and Galassi D 2023 *Nuclear Materials and Energy* **34** 101383 ISSN 2352-1791 URL <https://www.sciencedirect.com/science/article/pii/S2352179123000224>
- [41] C C, Moulton D and Lipschultz B 2024 *To be submitted*
- [42] Harrison J, Bowman C, Clark J, Kirk A, Lovell J J, Bhavin P, Ryan P, Scannell R, Thornton A J and Verhaegh K 2024 *EPS Conference, Plasma Physics Controlled Fusion, submitted*
- [43] You J, Mazzone G, Visca E, Greuner H, Fursdon M, Addab Y, Bachmann C, Barrett T, Bonavolontà U, Böswirth B, Castrovinci F, Carelli C, Coccorese D, Coppola R, Crescenzi F, Di Gironimo G, Di Maio P, Di Mambro G, Domptail F, Dongiovanni D, Dose G, Flammini D, Forest L, Frosi P, Gallay F, Ghidersa B, Harrington C, Hunger K, Imbriani V, Li M, Lukenskas A, Maffucci A, Mantel N, Marzullo D, Minniti T, Müller A, Noce S, Porfiri M, Quartararo A, Richou M, Roccella S, Terentyev D, Tincani A, Vallone E, Ventre S, Villari R, Villone F, Vorpahl C and Zhang K 2022 *Fusion Engineering and Design* **175** 113010 ISSN 0920-3796 URL <https://www.sciencedirect.com/science/article/pii/S0920379622000102>
- [44] Goldston R, McCune D, Towner H, Davis S, Hawryluk R and Schmidt G 1981 *Journal of Computational Physics* **43** 61–78 ISSN 0021-9991 URL <https://www.sciencedirect.com/science/article/pii/002199918190111X>
- [45] Kogan L, Gibson S, Ryan D, Bowman C, Kirk A, Berkery J, Sabbagh S, Farley T, Ryan P, Wade C *et al.* 2022 First mast-u equilibrium reconstructions using the efit++ code *48th European Physical Society Conference on Plasma Physics, EPS 2022* (European Physical Society (EPS)) URL <https://info.fusion.ciemat.es/OCS/EPS2022PAP/pdf/P2a.116.pdf>
- [46] Ryan P J, Elmore S D, Harrison J R, Lovell J and Stephen R 2023 *Review of Scientific Instruments* **94** 103501 ISSN 0034-6748 (*Preprint* https://pubs.aip.org/aip/rsi/article-pdf/doi/10.1063/5.0152680/18157571/103501_1_5.0152680.pdf) URL <https://doi.org/10.1063/5.0152680>
- [47] Derks G, Kool B, Vincent C, Elmore S, Henderson S, Koenders J, Lovell J, McArdle G, Parry B, Scannell R, Sarwar R, Verhaegh K and van Berkel M 2024 *Fusion Engineering and Design* **202** 114387 ISSN 0920-3796 URL <https://www.sciencedirect.com/science/article/pii/S0920379624002400>
- [48] Wiesen S, Reiter D, Kotov V, Baelmans M, Dekeyser W, Kukushkin A, Lisgo S, Pitts R, Rozhansky V, Saibene G, Veselova I and Voskoboinikov S 2015 *Journal of Nuclear Materials* **463** 480–484

8. Extended data

Discharge	R_t (m)	F_x	F_R	L (m)	L_{pol} (m)	Description
46860	1.45	9	2.3	19	1.3	Super-X Divertor (SXD)
47079	1.11	6	1.7	17	1.1	Elongated Divertor (ED)
46866	0.79	3.3	1.2	13	0.64	Conventional Divertor (CD)
46895	0.81 - 1.39	4 - 6	1.2 - 2.2	13 - 19	0.65 - 1.3	CD ->ED ->SXD scan

Table 1. Summary of the magnetic divertor shape parameters for the discharges discussed in this work, featuring target radius (R_t), poloidal flux expansion (F_x), total flux expansion (F_R), connection length (L) and poloidal leg length (L_{pol})

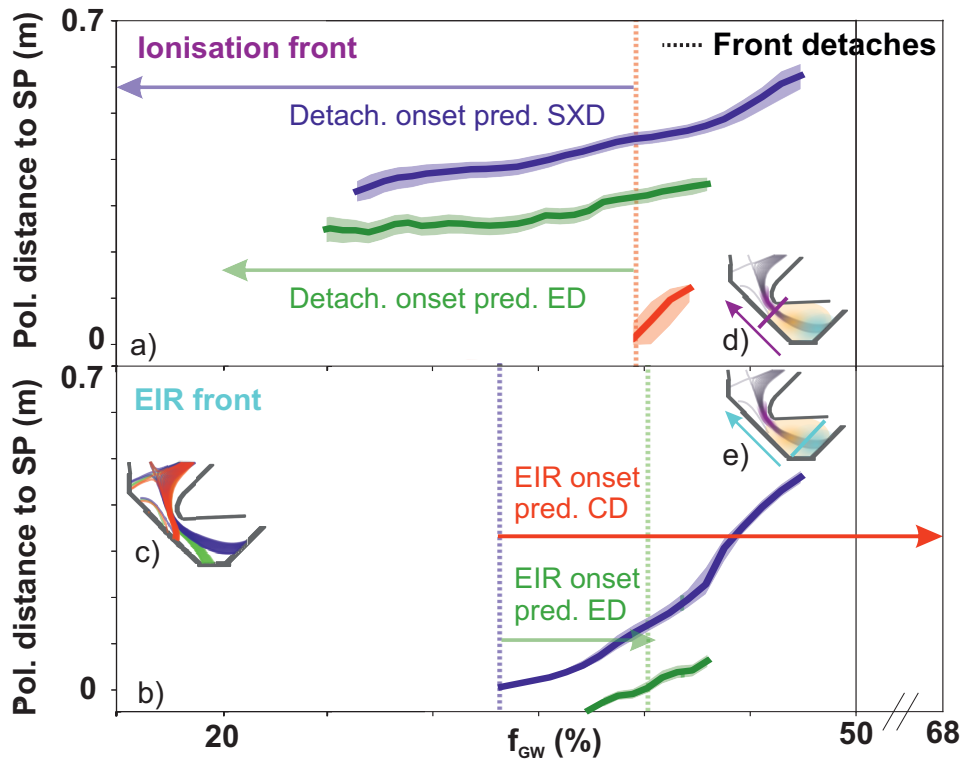


Figure 6. Detachment front evolution as function of f_{GW} , including comparisons against reduced models. Evolution of the ionisation front (a), EIR front (b), in terms of poloidal distance to the strike point, for the divertor geometries shown in c. Dotted lines are shown at the onset of the ionisation front movement and EIR appearance. Using the DLS model, the ionisation front detachment observation of the CD (a) and EIR appearance of the SXD (b) are rescaled to predictions for the SXD/ED and ED/CD respectively, indicated by shaded arrows. The X-axis of b) is extended to $f_{GW} = 68\%$ to indicate the predicted CD EIR onset. Illustrations of the ionisation front (downstream) and EIR front (upstream) are shown (d,e)

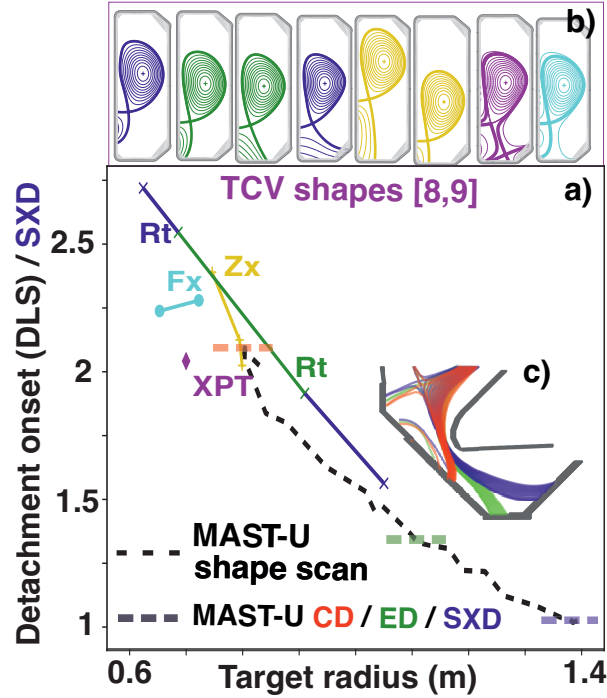


Figure 7. DLS model detachment onset predictions for various MAST-U and TCV divertor shapes, normalised to the MAST-U Super-X divertor. a) Detachment onset predictions as function of target radius for the MAST-U SXD, ED and CD, as well as the strike point scan of # 46895 (presented in Figure 5). DLS onset predictions for TCV from [16, 18] are also shown for a target radius scan (R_t), poloidal flux expansion scan (F_x), divertor leg-length scan (Z_x) and X-Point Target (XPT). Corresponding equilibria are shown for MAST-U (b) and TCV (c).

9. Methods

9.1. MAST Upgrade, Alternative Divertor Configurations and the Super-X Divertor

MAST Upgrade is a medium sized, small aspect ratio (i.e., spherical) tokamak (major radius: 0.9 m, minor radius: 0.6 m) operated by the United Kingdom Atomic Energy Authority [36]. It has a toroidal field of 0.8 T, its plasma current can reach up to 1 MA, and features one off-axis and one on-axis neutral beam external heating injection, of up to 2.2 MW per neutral beam. TRANSP simulations are used to model the neutral beam absorption, required to estimate the power entering the scrape-off-layer (SOL) [44]. MAST-U features core Thomson scattering to obtain core electron density and temperature profiles, uses far-infrared-reflectometry (FIR) to obtain the line-averaged electron density and utilises the magnetic equilibrium reconstruction code EFIT to reconstruct the magnetic equilibria based on magnetic probe measurements [45]. Its divertor is well diagnosed, featuring line-of-sight spectroscopy [8], imaging diagnostics [34], Langmuir probes [46], as well as an imaging bolometry system at the X-point [31].

In this work, fuelling injection from the low field side is used to maintain L-mode conditions whilst controlling the core density in real time with main chamber fuelling [47].

The advantage of using higher power L-mode conditions in this study is that the upstream density can be reduced compared to that in H-mode, lowering the detachment onset and enabling a wider range of upstream density scans to investigate the evolution during detachment.

MAST-U features upper and lower divertor chambers, enabling double null diverted scenarios. The divertor chambers prevent neutral transport from the divertor to the core, providing neutral baffling and contributing to core-edge compatibility. The large divertor chamber, combined with various divertor coils [37], facilitates the integration of complex divertor shapes with strong neutral baffling. This enables studying the impact of divertor shaping on power exhaust while maintaining strong neutral baffling.

With this shaping flexibility, MAST-U can alter the poloidal flux expansion, connection length and total flux expansion. Poloidal flux expansion, $F_x = \frac{B_\theta^u B_\phi^t}{B_\theta^t B_\phi^u}$ [16], is the ratio of the perpendicular flux surface spacing at the target and upstream, where $B_{\theta,\phi}^{u,t}$ are the poloidal (θ) and toroidal (ϕ) components of the magnetic field at upstream (u) and at the target (t), respectively. Increasing F_x reduces the target heat loads (W/m^2) by spreading it over a larger surface. Increasing the connection length between the midplane and the divertor target (L_{\parallel}), provides a larger radiating volume and is expected to improve power exhaust [16]. Total flux expansion ($F_R = \frac{B_{xpt}}{B_t}$) increases the cross-sectional area of a flux tube, spreading the heat over a larger radius and lowering the target temperature [16, 20]. The spherical nature of MAST-U enables varying total flux expansion over an unprecedented range, making it an ideal testbed for studying the impact of total flux expansion in a strongly baffled divertor.

9.2. Divertor detachment, ion source/sink inferences and power balance

Power exhaust can be facilitated by plasma detachment, which is a state where simultaneous power, particle and momentum losses result in a simultaneous reduction of target particle fluxes and plasma target temperature.

Using novel spectroscopic techniques [7, 8] of hydrogen atomic Balmer line emission, the electron temperature, ion sources (I_i) and sinks (I_r) from plasma-atom and molecular interactions, as well as the hydrogenic radiative power losses and Molecular Activated Dissociation, can be inferred from the hydrogen Balmer line emission.

Since the line-of-sight spectroscopy system has a set fan of views throughout the divertor leg (Figure 1), spatial profiles of chordally integrated ion sources and sinks along the divertor leg can be obtained (Figure 3 d,e,f). During detachment, first the ionisation source detaches from the target ($T_e < 3 - 5$ eV, inferred spectroscopically [8]) and ultimately Electron-Ion Recombination (EIR) starts to occur near the target ($T_e \approx 0.2$ eV, $n_e \approx 2 - 4 \times 10^{19} \text{m}^{-3}$, according to spectroscopic inferences of the high- n ($n > 9$) Balmer line spectra [9]). By tracking the location of the downstream-end of the ionisation source ($(1.5 \pm 0.25) \times 10^{21} \text{part}/\text{m}^2/\text{s}$) and the upstream-end of the EIR sink ($(3 \pm 0.5) \times 10^{20} \text{part}/\text{m}^2/\text{s}$), the distance between the target and the ionisation front (defined as the detachment front) and EIR front (colder reference point of deeper

detachment) can be obtained. These numbers are obtained as onset points based on the spatial profiles of ion sources and sinks presented in Figure 2 (d).

Combining spectroscopic inferences on ion sources and sinks with Langmuir probe measurements, information on both particle and power balance can be obtained.

The total ion target flux (I_t in part./s) is obtained by integrating the ion target flux Γ_t (part/ m^2 /s) measured by Langmuir probes. From conservation of particles, the total ion target flux should equal the ion sources minus the ion sinks, in addition to any net ion inflow into the monitored system I_u , Equation 1. Using particle balance, the total ion source ($I_i + I_u$) can be inferred by adding the ion target flux and the ion sinks.

$$I_t = I_i - I_r + I_u \quad (1)$$

The target power loading can be inferred using a combination of spectroscopy and Langmuir probe measurements. To overcome limitations of estimating target temperatures using Langmuir probes in low temperature conditions [46], spectroscopy from lines-of-sight closest to the target is used to infer a characteristic target electron temperature T_t . Using this temperature, the perpendicular plasma target power deposition can be estimated as $P_{\perp,target} = I_t(\gamma T_t + \epsilon)$ (in W), whereas the peak perpendicular heat flux can be estimated as $q_{\perp,peak} = \Gamma_{t,peak}(\gamma T_t + \epsilon)$ (in W/ m^2). A sheath transmission factor of $\gamma = 7$ is assumed (valid for equal electron and ion temperatures) and both surface recombination and molecular re-association is accounted for in the potential energy $\epsilon = 13.6 + 2.2$ eV.

Assuming that all volumetric power losses are purely due to hydrogenic radiation as well as dissociation, which is motivated by the observation that hydrogenic radiation estimates from spectroscopic analysis align with the measured total radiation in these conditions [27], the power into the divertor chamber can be estimated by summing $P_{\perp,target}$ and the inferred hydrogenic divertor radiative power loss.

Although this does include surface recombination, it does not include target heat loads due to photons and neutral atoms. Including dissociation as a total loss channel implies assuming that the neutral atoms, after dissociation, are mostly lost to the side walls, rather than reaching the target (and hence do not contribute as target heating), which is consistent with findings in SOLPS-ITER simulations.

9.3. Detachment Location Sensitivity (DLS) model

The Detachment Location Sensitivity (DLS) analytical model [20, 32, 33] can model the impact of the magnetic divertor geometry on the detachment threshold in terms of upstream density n_u , impurity fraction f_z and parallel heat flux q_{\parallel} ($C_t \propto \frac{n_u \sqrt{f_z}}{q_{\parallel}^{5/7}}$), as shown in Equation 2, where purely the magnetic geometry dependencies have been extracted from the DLS model [33]. In here, B is the total magnetic field, ξ is the coordinate representing the volume of the flux tube between the target and a given

position along the divertor leg, scaled by a reference area $\propto 1/B_{xpt}$.

$$C_t \propto \frac{B_t}{B_{xpt}^{3/7}} \times \left(\int_t^{xpt} B^2(\xi) d\xi + \int_{xpt}^u B^2(\xi) \left(\frac{L - \xi}{L - \xi_{xpt}} \right) d\xi \right)^{-2/7} \quad (2)$$

The advantage of this formulation is that it considers the full magnetic field dependency numerically, rather than approximating the field variation as linear with ξ . Under those approximations, Equation 2 can be simplified as: $C_t \propto \frac{B_t}{B_{xpt}} \left(\frac{B_{xpt}}{\langle B \rangle} \right)^{2/7} \frac{1}{L_{\parallel}^{2/7}}$ [32]. The DLS model thus predicts that detachment onset is facilitated by increased connection length (L_{\parallel}) and increased total flux expansion $\frac{B_t}{B_{xpt}}$. We find negligible differences between this approximate form and the full numerical calculation for the MAST-U shapes reported in this work. The DLS model is applied to a flux tube that is 0.5 mm outwards of the separatrix into the SOL, to avoid numerical errors.

The DLS model formally assumes that all power is dissipated by impurity radiation and that the radiating specie has a constant concentration in the radiating region. This is likely not the case in the MAST-U divertor chamber where the radiative power losses are dominated by hydrogenic interactions [8]. However, the impact of the divertor topology on the detachment onset appears to be more generally applicable outside of impurity radiation dominant conditions. Assuming the impurity fraction is constant and that the upstream electron density and heat flux are proportional to, and fully determined by, f_{GW} and P_{SOL} , the detachment threshold is expected to be dependent on $C_t \propto \frac{n_u}{q_{\parallel}^{5/7}} \propto \frac{f_{GW}}{P_{SOL}^{5/7}}$. The DLS model predictions in Figure 6 account for the change in P_{SOL} during the experiment (Figure 2a).

9.4. Exhaust simulations - SOLPS-ITER

Reduced models, such as the Detachment Location Sensitivity (DLS) model, are useful for building a physics understanding. However, the divertor behaviour is highly complex: it is a 2D/3D phenomena that involves interactions between the plasma with neutral atom and molecules. SOLPS-ITER is a state-of-the-art code suite for advanced power exhaust modelling [48]. It combines a fluid code with a Monte Carlo neutral code that tracks the neutrals and incorporates several atomic and molecular databases [48].

Interpretive SOLPS-ITER simulations have been performed using a baseline SOLPS-ITER setup that has been matched against Ohmic experimental data [19]. These simulations have been extrapolated to the higher power experiments presented here, using corresponding experimental magnetic equilibria, fuelling location, and P_{SOL} . The fuelling rate has been tuned in order to match the experimentally measured upstream electron densities.